In-line phase-contrast breast tomosynthesis: a phantom feasibility study at a synchrotron radiation facility

In-line phase-contrast breast tomosynthesis: a phantom feasibility study at a synchrotron radiation facility

K Bliznakova[1], **P Russo**[2], **Z Kamarianakis**[4], **G Mettivier**[2], **H Requardt**[3], **A Bravin**[3] **and I Buliev**[1]

[1] Department of Electronics, Technical University of Varna,
1 Studentska Str, Varna, 9010 Bulgaria
[2] Dipartimento di Fisica, Università di Napoli Federico II,
and INFN Sezione di Napoli, Via Cintia, I-80126, Naples, Italy
[3] European Synchrotron Radiation Facility (ESRF), Grenoble F-38043, France
[4] Department of Medical Physics, University of Patras, Patras, 26500, Greece

E-mail: kristina.bliznakova@tu-varna.bg

CrossMark

Abstract

The major objective is to adopt, apply and test developed in-house algorithms for volumetric breast reconstructions from projection images, obtained in in-line phase-contrast mode.

Four angular sets, each consisting of 17 projection images obtained from four physical phantoms, were acquired at beamline ID17, European Synchroton Radiation Facility, Grenoble, France. The tomosynthesis arc was $\pm 32°$. The physical phantoms differed in complexity of texture and introduced features of interest. Three of the used phantoms were in-house developed, and made of epoxy resin, polymethyl-methacrylate and paraffin wax, while the fourth phantom was the CIRS BR3D. The projection images had a pixel size of $47~\mu\text{m} \times 47~\mu\text{m}$. Tomosynthesis images were reconstructed with standard shift-and-add (SAA) and filtered backprojection (FBP) algorithms.

It was found that the edge enhancement observed in planar x-ray images is preserved in tomosynthesis images from both phantoms with homogeneous and highly heterogeneous backgrounds. In case of BR3D, it was found that features not visible in the planar case were well outlined in the tomosynthesis slices. In addition, the edge enhancement index calculated for features of interest was found to be much higher in tomosynthesis images reconstructed with FBP than in planar images and tomosynthesis images reconstructed with SAA. The comparison between images reconstructed by the two reconstruction algorithms shows an advantage for the FBP method in terms of better edge enhancement.

Phase-contrast breast tomosynthesis realized in in-line mode benefits the detection of suspicious areas in mammography images by adding the edge enhancement effect to the reconstructed slices.

Keywords: breast tomosynthesis, phase-contrast, filtered backprojection, shift-and-add reconstruction, inhomogeneous background

(Some figures may appear in colour only in the online journal)

1. Introduction

Digital breast tomosynthesis (DBT) is a promising three-dimensional (3D) x-ray imaging modality already used in daily clinical practice for breast cancer screening (Sechopoulos 2013). Several studies have shown that the addition of DBT to digital mammography is associated with a decrease in recall rate and an increase in cancer detection rate (Friedewald *et al* 2014, Durand *et al* 2015). The technique allows the partial removal of the influence of overlapping tissues, which is intrinsic to two-dimensional (2D) mammography and may lead to improved breast cancer visualization. Typically, DBT uses 9–25 projection images of the breast acquired with dedicated x-ray based mammography systems. The spatial resolution of DBT is in the order of $0.1\,\text{mm} \times 0.1\,\text{mm} \times 1\,\text{mm}$ ($x \times y \times z$), whereas digital mammography has a resolution in the order of $0.1\,\text{mm} \times 0.1\,\text{mm} \times 50\,\text{mm}$. Each projection image requires only a fraction of the total dose of a full 2D mammogram because all of the projection images are added together to synthesize the tomographic planes (Kopans 2014).

While cone beam breast computer tomography (CT) with dedicated scanners is a fully 3D technique for breast imaging, which produces isotropic resolution (Sarno *et al* 2015), in DBT the various views are input to reconstruction algorithms to provide a pseudo 3D image of the breast. However, DBT (as well as breast CT) is based on projections acquired in absorption mode, where x-ray images are formed from local variations in the absorption properties of the various breast tissues. In this imaging modality, the tumor contrast in projection images (with respect to background fibroglandular tissue) is less than 10%, typically, since the values of the x-ray attenuation coefficient $\mu(E)$ of normal (fibroglandular) and cancerous breast structures (like invasive/non-invasive ductal and lobular carcinoma) differ by only a small percent at most, in the photon energy range of 15 keV–110 keV.

One approach to increase tumor and microcalcification contrast in tomosynthesis images is by using phase-contrast (PhC) projection images in the tomosynthesis setup instead of images acquired in attenuation mode. Grating-based PhC and in-line PhC experimental arrangements were recently reported as approaches that may be used to produce PhC images. In the case of grating-based PhC tomosynthesis, Schleede *et al* (2014) presented for the first time results from a tomosynthesis of a 9 mm thick mastectomy sample section characterized by an invasive ductal carcinoma. PhC tomosynthesis slices showed improved visibility of fibrous structures in comparison to absorption-based tomosynthesis; moreover, some tissue structures were visible only in PhC tomosynthesis images. In the same line of research, Li *et al* (2014) reported on a PhC tomosynthesis study realized with 21 projection images obtained for each of the three in-house developed physical objects with known $\mu(E)$ and $\delta(E)$ characteristics. Both the filtered backprojection method (FBP) realized with a Hilbert kernel and a shift-and-add algorithm (SAA) were used as the reconstruction algorithms. They concluded that neither of the reconstruction methods, applied in their studies, can be used to replace absorption-based tomosynthesis. Moreover, the authors suggested that absorption and PhC mechanisms provide complementary information. Another study, reported by Szafraniec *et al* (2014), showed that a

strong PhC signal is preserved in tomosynthesis images obtained from a 'double TORMAM' phantom with a total thickness of 3.2 cm in their coded-aperture based laboratory implementation of x-ray PhC tomosynthesis. Phantom details of interest were clearly isolated, while a strong PhC signal was preserved at the edges of the details in tomosynthesis images, reconstructed by an iterative algorithm. The studies of Li *et al* and Szafraniec *et al* however, concerned phantoms with a homogeneous background.

The in-line (or propagation-based) implementation of PhC tomosynthesis has also been reported (Hammonds *et al* 2011, Ikeya *et al* 2013, Guan *et al* 2014a). In this technique, no optical elements like apertures or gratings are used in the beam path for x-ray acquisitions. Arrangements included experimental systems either in a laboratory or at synchrotron facilities, and polymethyl-methacrylate (PMMA) phantoms with features of interest imaged in PhC tomosynthesis conditions. The reconstruction algorithms used in these studies were FBP and SAA. The PhC tomosynthesis images retained the edge enhancement effects observed in the planar projection images of simple PMMA phantoms. More recently, Guan *et al* (2014b) showed through simulations that x-ray PhC tomosynthesis provides better *z*-resolution than conventional DBT. The authors used an advanced iterative algorithm with PhC images simulated within an angular arc of 40°.

These preliminary studies, although carried out with simple phantoms, point out the potential benefits of applying x-ray PhC tomosynthesis for imaging the breast, in the simple geometry of in-line PhC imaging. They also motivate the further development and optimization of this technique as well as its clinical application towards the successful detection of suspicious regions in mammography images and the better differentiation of breast structures. The use of more complex and thicker phantoms is necessary for this purpose.

In this work the authors adopt, apply and test in-house developed algorithms for volumetric breast reconstructions from PhC projection images, obtained in an in-line PhC tomosynthesis setup. The investigative goal is to test whether enhanced edges of image details (including breast-like lesions)—produced by PhC with a highly coherent, monochromatic x-ray source—are preserved in tomosynthesis reconstructed images of phantoms characterized by different structural complexity. The specific objectives of the study are: (a) to demonstrate the ability to synthesize tomosynthesis images of varying-complexity phantoms, which are built from materials mostly having characteristics close to the absorption and the refractive characteristics of real breast tissue using a PhC setup at a synchrotron facility; (b) to apply and compare in-house developed 3D algorithms for the reconstruction of PhC tomosynthesis slice images devised for x-ray breast imaging; and (c) to evaluate the amount of edge enhancement effects in PhC tomosynthesis images for the tested reconstruction algorithms.

Experiments were carried out at the European Synchrotron Radiation Facility (ESRF) (Grenoble, France) using four physical phantoms made of materials commonly utilized in the construction of phantoms in x-ray diagnostic imaging. PhC tomosynthesis was implemented by acquiring 17 angular views of these phantoms within an angular span of $\pm 32°$; tomosynthesis slices were reconstructed by the standard SAA and FPB algorithms. Furthermore, the reconstructed slices were compared to the corresponding planar images in terms of feature visibility and sharpness.

2. Materials and methods

2.1. Phantoms

Four physical phantoms of varying composition and complexity were used in the study (figure 1): (a) *PMMA phantom* (phantom 1)—a homogeneous PMMA sample in the form of a slab of size 6 cm $\times$ 6 cm $\times$ 4 cm through the smallest face of which four air-filled cylindrical holes
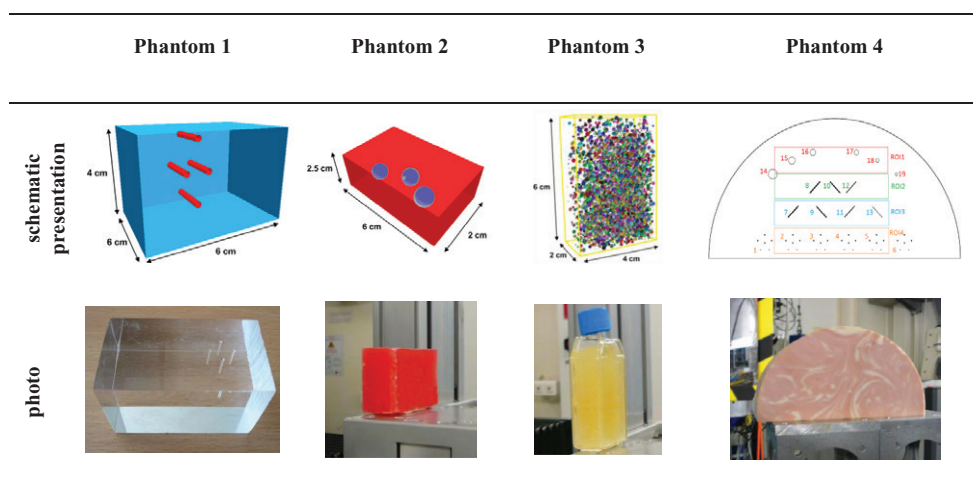
Figure 1. Phantoms used in the experimental study. Phantoms 1 and 2 are homogeneous slabs embedding test objects inserted at different positions as shown in the first row. They were used for initial evaluation of the reconstruction algorithms. Phantoms 3 and 4 represent complex phantoms dedicated to test the performance of PhC tomosynthesis with objects characterized by an inhomogeneous texture. The ROIs under investigation for phantom 4 are noted on its schematic presentation as ROI1 to ROI4.

(diameter of 1 mm) were drilled vertically; (b) *paraffin phantom* (phantom 2)—a homogeneous paraffin slab of size 6 cm × 4 cm × 2.5 cm, containing three water spheres (diameter of 0.8 cm), placed at different depths in the slab; (c) *epoxy resin phantom with air bubbles* (phantom 3)—a rectangular polystyrene flask with size 6 cm × 4 cm × 2 cm filled with an epoxy resin mixture and then shacked in order to produce a large number of air sacs of different sizes; and (d) *CIRS model 020 BR3D* (phantom 4)—five slabs stacked together to simulate a 5 cm thick compressed breast with tissue composition of 50% glandular–50% adipose (CIRS Inc., Norfolk). The central slab of the stack contains details simulating microcalcifications, fibers and masses.

The first row in figure 1 shows a schematic representation of the phantoms used in this study, while the second row shows photos of the physical phantoms used in the experimental work. The linear attenuation coefficients and the refractive indices of the materials used in the experimental work are summarized in table 1. For comparison purposes, we provide the corresponding coefficients for breast tissues as well.

The refractive index decrements (δ) for four of the materials in table 1 were taken from the CSIRO Imaging portal. The refractive index decrement for the rest of the materials is calculated by taking into account that $\delta = N_e(r_e\lambda^2)/2\pi$, where r_e is the classical electron radius, while N_e is the electron density of the tissue and λ is the wavelength. For each element and composition, N_e is calculated, knowing the chemical formula for each material simulated. The linear attenuation coefficients for these materials were taken from the XCOM database (Berger *et al* 2010).

2.2. Experimental setup

The experiment was conducted at the biomedical beamline ID17 at the ESRF (Bravin *et al* 2007). Coherent radiation is obtained from the wigglers of the storage ring. A monolithic channel-cut Si (1 1 1) crystal is placed 153 m from the source to produce a monochromatic beam, with energy selectable in the range 25–140 keV. A tungsten slit system, located approximately

Table 1. Elemental composition as percentage weights, density, linear attenuation coefficient and refractive index decrement of materials used in the study for 35 keV.

Material	Composition	Density, g cm^{-3}	Linear attenuation coefficient, μ cm^{-1}	Refractive index, δ
PMMA[a]	H: 0.080; C: 0.600; O: 0.320	1.19	0.31	2.18×10^{-7}
Paraffin	H 0.150; C: 0.850	0.93	0.23	1.81×10^{-7}
Epoxy resin	H: 0.070; C: 0.740; O: 0.190	1.10	0.31	2.45×10^{-7}
H$_2$O[a]	H: 0.110; O: 0.890	1.00	0.31	1.88×10^{-7}
Adipose[a]	H: 0.119; C: 0.637; N: 0.008; O: 0.232; Na: 0.001; P: 0.0002; S: 0.0007; Cl: 0.001; K: 0.0003	0.92	0.24	1.75×10^{-7}
Gland[a]	H: 0.106; C: 0.332; N: 0.030; O: 0.527; Na: 0.001; P: 0.001; S: 0.002; Cl: 0.001	1.02	0.31	1.94×10^{-7}

[a] Data taken from CSIRO Imaging portal (https://ts-imaging.net/Default.aspx).

150 m from the source, collimated the beam cross section to a size of 150 mm × 6 mm; the photon energy for the experiments was 35 keV.

The detector was a tapered optics FReLoN 2k CCD camera, a fast-readout and low-noise charge-coupled device with a pixel size of 47 μm and a field-of-view of 95 mm × 95 mm. It was located at a distance of 11 m downstream of the beam exit surface of the phantom. Further, the FReLoN camera was placed on a fixed platform and the phantoms were mounted horizontally on a motorized scanning stage that could rotate around a vertical axis and translate vertically. Images for tomosynthesis were obtained by the following setup. Each phantom was scanned by rotating the phantom stage in a full arc of 360° and projection views were recorded every 4°. From the whole set of 90 images, 17 projection images were used for tomosynthesis, in an arc from −32° to +32°, where 0° is the direction normal to one of the largest faces of the phantom slab. Due to the limited vertical extent of the beam (6 mm), in order to scan the whole height of the phantom its supporting platform was translated vertically at the end of each full rotation, in a rotate–translate sequence. Depending on the phantom's height, the number of vertical scans varied. The size of the recorded images was 2048 (width) × 93 (height) pixels. The whole projection image was then obtained by combining the different images acquired in a single vertical step; for phantom 1, the image size was 2048 × 1003 pixels; for phantom 2, 2048 × 1062 pixels; for phantom 3, 2048 × 236 pixels; and for phantom 4, 2048 × 2242 pixels. The incident air kerma per single projection image was 0.33 mGy, while the exposure duration was 26 ms.

2.3. Projection data processing and reconstruction algorithms used

Tomosynthesis images were reconstructed with an in-house developed reconstruction platform (Kamarianakis *et al* 2014). The PIRXI software platform (platform for image reconstruction in x-ray imaging) is a tool based on the RTCL, Reconstruction Techniques Class Library, which is another in-house developed object-oriented library for x-ray based applications (Kamarianakis *et al* 2013). This platform permits the fast development of known image reconstruction algorithms based on various projection data from known image acquisition setups (e.g. CT, tomosynthesis, etc) and the programming and testing of new reconstruction techniques, using modified or new projection acquisition trajectories. The core components of the platform are C++ classes that provide the user with software equivalents

of a real CT imaging chain (e.g. x-ray source, flat-panel detector, image reconstruction processor, etc). By combining instances of these classes with the appropriate methods on projection data (e.g. filtering, 3D transformations) the user can repeat and simulate a large variety of imaging setups and eventually use the processed images to reconstruct objects at arbitrary orientations.

Two basic algorithms, the SAA and the FBP algorithm, are fully implemented in the platform. Both line integrals and x-ray intensity images can be used to reconstruct tomograms. Different types of filters may be selected for the FBP algorithm. The geometry may be isocentric rotational and partially isocentric (stationary detector). The parameters adjusted for the algorithms to reconstruct tomograms from PhC projections mainly concerned the geometry (rotating object, stable source and detector), as the deviation and the actual position of the detector with respect to the axis of the object rotation were accurately identified from the acquired projection images and taken into account in the reconstructions.

For the purposes of this study, the size of the in-plane reconstructed voxels was set to 43.6 μm × 43.6 μm. The voxels were considered anisotropic, by means of slice separation. Slice thickness was set to 0.1 mm. The images were reconstructed with both the SAA and FBP algorithms. Advanced iterative techniques were not considered at this stage. A detailed comparison and optimization of the algorithms, including iterative-based methods, will be performed in follow-up experimental and simulation studies on the tomosynthesis images of anthropomorphic breast phantoms with known realistic breast tissue distribution. In the case of FBP, prior to reconstruction, the projection images were pre-processed with a modified ramp filter kernel. The required Ram–Lak filter was combined with an apodization window to suppress the highest-frequency components and reduce the influence of random noise while keeping an optimal spatial resolution loss. No other pre-processing (e.g. denoising methods) was applied prior to backprojection in all cases. The reconstructed set of images varied from 400 slices for phantoms 1 and 2, to 500 slices for phantoms 3 and 4 in order to cover the volumes of interest.

2.4. Evaluation of image quality

To quantify differences in the conspicuity of the edge enhancement effect of objects in the reconstructed and projection images, the edge enhancement index (EEI) and the edge enhancement to noise ratio (EE/*N*) adopted by Donnelly *et al* (2006) were used:

$$\text{EEI} = \frac{(P - T)/(P + T)}{(H - L)/(H + L)} \qquad \text{EE/}N = \frac{P - T}{\sqrt{\sigma_H^2 + \sigma_L^2}}$$

where P and T are the peak and the trough intensity value at the edge, respectively; H and L are the intensity values that would result at these locations if there were no edge enhancement at the high- and low-intensity regions next to the edge. The H and L values were calculated for a square region of size 100 × 100 pixels near the corresponding edge. σ_H and σ_L represent the standard deviation of the pixels in the region of interest used to calculate the H and L values, respectively. The first metric, the EEI, was used to quantify the edge enhancement effect relative to the absolute change in intensity from absorption differences across the edge, while the second metric, EE/*N*, was utilized to quantify the enhancement relative to the image noise.

In addition to the quantitative assessment, a task-based evaluation was designed for the images which belonged to the experiment with the CIRS model 020 BR3D. The study included three radiologists with more than 10 years of experience in the field of radiology and 17 slides with images representing regions of interest (ROIs) extracted from a planar image

and reconstructed images with FBP and SAA. The first slide contained the schematic image of phantom 4 with the four ROIs. It is followed by four slides per ROI: the ROI reconstructed by FBP, the ROI reconstructed by SAA, the planar ROI, and a slide containing all three ROIs.

In the case of masses, the observers were told that there were four masses with different sizes. The observers were asked to estimate the number of masses they see for each modality. In addition, they were asked to use grades from 1 to 5 for each of the masses: 1 (clearly absent), 2 (probably absent), 3 (present or absent), 4 (probably present), 5 (clearly present). For the microcalcifications, the observers were told that in the images there existed six microcalcifications per group with different sizes. They were asked to estimate the number of microcalcifications they see for each group, as well as to evaluate their visibility by using scores between 1 and 5. Similar guides were given with respect to the nylon fibers with different sizes.

3. Results and discussion

3.1. PhC tomosynthesis with simple homogeneous objects (Phantom 1, 2)

3.1.1. PMMA phantom (phantom 1).   Figure 2 shows the projection images of phantom 1, corresponding to the view at 0°, and figure 3 shows the corresponding tomosynthesis images reconstructed from the 17 acquired projection images of phantom 1 with the two tomosynthesis algorithms, relative to the phantom sections containing the air channels.

The projection image shown in figure 2(a) is the image obtained at an object-to-detector distance of 11 m (where significant PhC and edge enhancement effects are expected), while the image shown in figure 2(b) is the view obtained at an object-to-detector distance of 17 cm (where very minimal, or no, PhC and edge enhancement effects are expected due to the short propagation distance behind the object). The horizontal line profiles taken across these images are also shown. In both the PhC and absorption projection images (figures 2(a) and (b)), there is a complete overlap of two of the air-filled cylindrical holes embedded in the middle region of the phantom (see figure 1, phantom 1, for which the x-ray beam enters from the top). By contrast, on the tomosynthesis reconstructed slices (figure 3), all four air cavities are completely resolved and fully separated.

The reconstructed tomosynthesis images suffer from a strong artifact pattern, caused by the backprojected values of the edges of the out-of-plane phantom structures (for the used phantom these are the other cylinders and the phantom shape itself). This is a known effect, which in the case of PhC imaging is further enhanced. The nature of the artifacts is better presented in figure 4, which shows an axial reconstruction slice through the four cylindrical holes. However, the tomosynthesis images have an obvious advantage compared to the planar images—despite the strong strike artifacts, one can clearly differentiate the four air-filled cylinders and accurately determine their position in the PMMA phantom.

The EEIs and edge enhancement to noise ratios were calculated for each cylinder edge and subsequently these were averaged and shown at the top of the plot profiles. The edge enhancement effect, observed on the projection image in figure 2(a), is fully preserved on all tomosynthesis images, and it is even more pronounced: the EEI in the projection image (figure 2(a)) is 4.43 and increases to 36.64 and 42.09 in the tomosynthesis slices reconstructed with the FBP algorithm, while the EEIs for the projection images and SAA tomosynthesis slices are similar. In the case of SAA, the EEI is slightly reduced compared to the EEI calculated for the projection image, due to the weighting sum of the pixel values from the unfiltered projection images. In general, in the tomosynthesis images obtained with SAA, the improved object edges from the projections are preserved. The applied high-pass filter in the case of
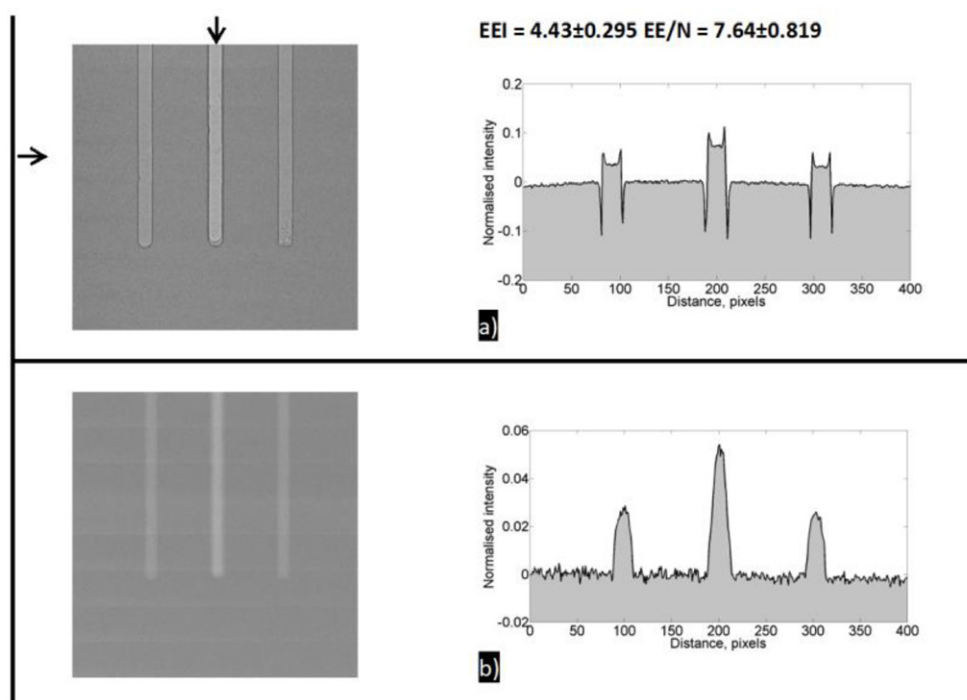
Figure 2. Projection images of the PMMA phantom with the four air-filled cylindrical holes (phantom 1): (a) projection image acquired in PhC arrangements (at 11 m distance); (b) projection image acquired at object-to-detector distance of 17 cm. The short arrow at the top of the projection image in (a) indicates the position of the two superimposed cylindrical holes along the beam direction. The line profiles shown on the right side of each image are taken at a level in the image as shown by the arrow on the left side in image (a).

FBP further enhances the object edges leading to improved edge visibility and higher EEI in the tomosynthesis images.

The lowest noise values (the *N* in EE/*N*) are obtained for the images reconstructed with SAA and for the planar projection images, while the highest are calculated for the FBP tomosynthesis slices. The latter mostly come from out-of-plane artifacts, which for the case of FBP are extremely pronounced, compared to SAA. However, due to the high EEI, the EE/*N* for the SAA slices is also retained at high levels: the EE/*N* index increases from 7.64 for the planar images (figure 2(a)) to 23.57 for the tomosynthesis images reconstructed with FBP (figure 3(d)). This EE/*N* improvement also occurs for the reconstructed SAA images. In the case of SAA, the out-of-plane edges are smeared which results in lower noise levels in the reconstructed images.

Similar results in terms of retained edge enhancement effects and EE/*N* improvement were claimed to be obtained by Hammonds *et al* (2011) in their experimental work with a cylindrical phantom containing three holes drilled within it with a diameter of 2 mm, even though they used neither the SAA nor the FBP algorithm but the multiple projection algorithm developed by Kolitsi *et al* (1992). The comparison of the two reconstruction algorithms SAA and FBP shown in figure 3 indicates an increased contrast of the reconstructed objects (in terms of EEI) for the FBP and reduced noise influence in the tomosynthesis slices reconstructed by both algorithms (in terms of EE/*N*). Szafraniec *et al* (2014) also found that their edge-illumination
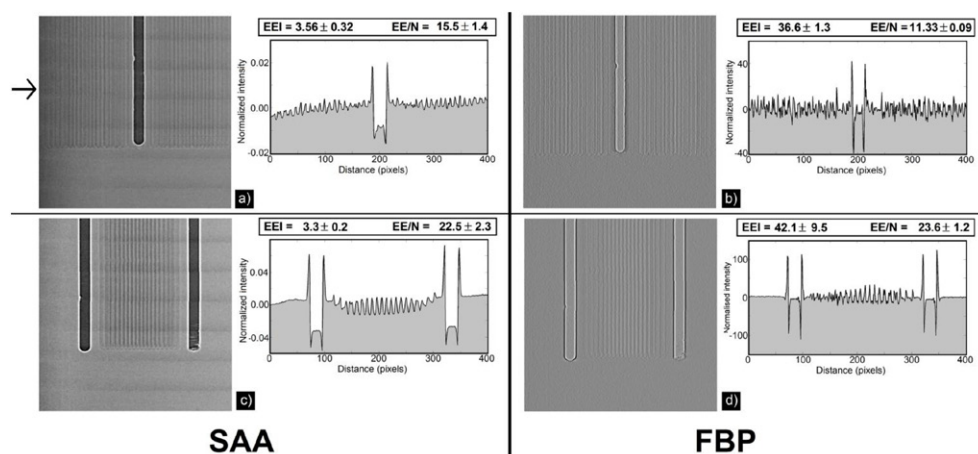
Figure 3. Tomosynthesis images (calculated from PhC projections), and corresponding horizontal line profiles (taken at a level as shown by the arrow on the left), of the PMMA phantom with the four air-filled cylindrical holes (phantom 1): panels (a) and (c) show two reconstructed planes by using SAA, while panels (b) and (d) show the corresponding slices reconstructed by the FBP algorithm. The planes are at heights in the phantom containing one and two cylindrical holes in focus, respectively.
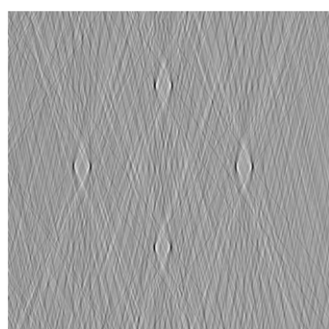

Figure 4. An axial slice taken through all four cylinder holes.

PhC tomosynthesis setup preserved the edge enhancement observed in planar images even though the effect was not expressed in quantitative terms.

3.1.2. Paraffin phantom (phantom 2).   Figures 5(a)–(d) show two reconstructed tomosynthesis slices from PhC projections of phantom 2 by using the SAA ((a), (b)) and FBP ((c), (d)) algorithms. The selected slices are the central planes which pass through the middle ((a), (c)) and leftmost ((b), (d)) water spheres, respectively. The tomosynthesis slice in ((b), (d)) is the central slice that passes through the leftmost sphere and at the same time corresponds to a slice that is 2 mm away from the central slice that passes through the middle sphere ((a), (c)). For comparison purposes, figures 5(e) and (f) show the projection images, which correspond to images of phantom 2 taken at 0° (central view) and object-to-detector distances of 11 m and 17 cm, respectively. Line profiles taken across the spheres are shown in each sub-panel of figure 5. As in the case of phantom 1, the EEIs calculated for the edges of the central sphere (figure 5(c), EEI = 91.43 and EE/N = 34.02) and of the left sphere (figure 5(d), EEI = 50.76
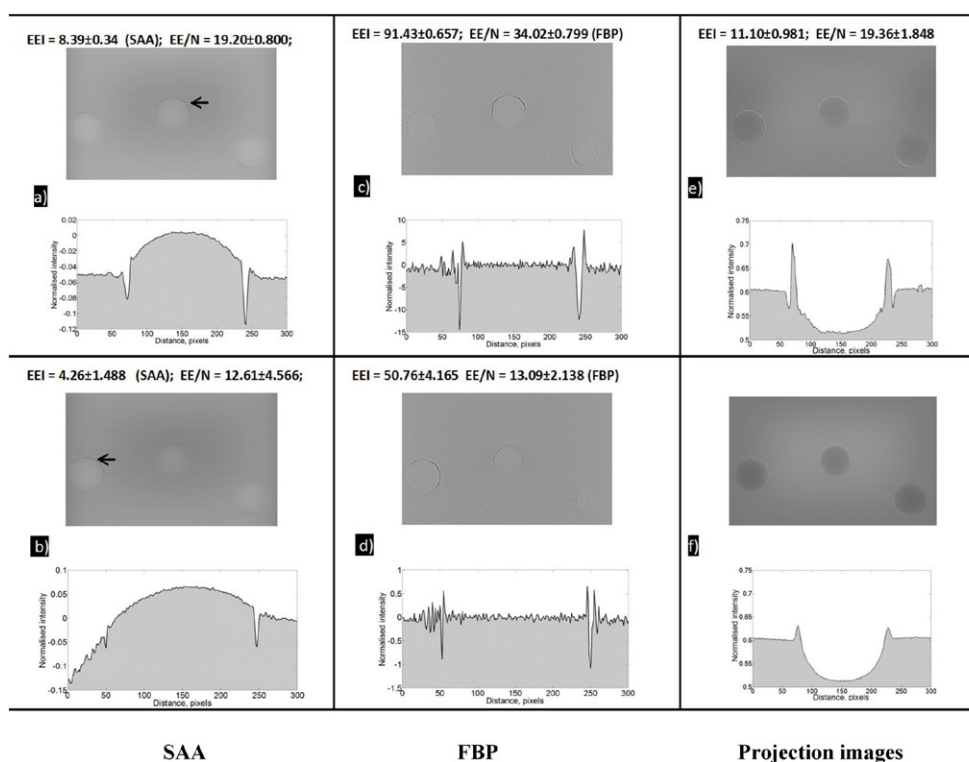
Figure 5. Comparison of reconstructed and planar images of the paraffin phantom (phantom 2). Selected reconstruction planes containing, respectively, the central ((a) and (c)) and the leftmost ((b) and (d)) sphere of the three spheres embedded in this phantom; (e) projection image at 11 m distance from the detector and corresponding line profile; (f) projection image at 17 cm distance from the detector. The reconstruction planes are taken through the center of the spheres. The line profiles across the sphere are shown below each image in the panels. The images in ((a) and (b)) are reconstructed with SAA, while the images in ((c) and (d)) are reconstructed with the FBP algorithm. The arrows in images (a) and (b) show the level at which the line profiles were taken.

and EE/N = 13.09) for the case of FBP were higher than the corresponding indices calculated for these details in the PhC projection image (figure 5(e), EEI = 11.10 and EE/N = 19.36), and tomosynthesis images obtained with SAA (figure 5(a), EEI = 8.39 and EE/N = 19.20; figure 5(b), EEI = 4.26 and EE/N = 12.61).

This finding, and the similar results obtained in the previous section for the two experimental trials with simple phantoms incorporating a homogeneous background, showed that the edge enhancement effect observed for features in PhC planar imaging is preserved, for the case of PhC tomosynthesis. The comparison between the two algorithms shows an advantage for the FBP approach in terms of better sharpness of the features' outline, as compared to the simple backprojection operation delivered by the SAA algorithm. This is also confirmed by the EEI and EE/N comparison between the SAA and FBP images. The comparison shows that FBP results in a higher EEI which objectively confirms the visually observed more enhanced object edges in slices obtained by FBP compared to those obtained with SAA. This outcome is expected, in a certain degree, since SAA uses unfiltered projection images.
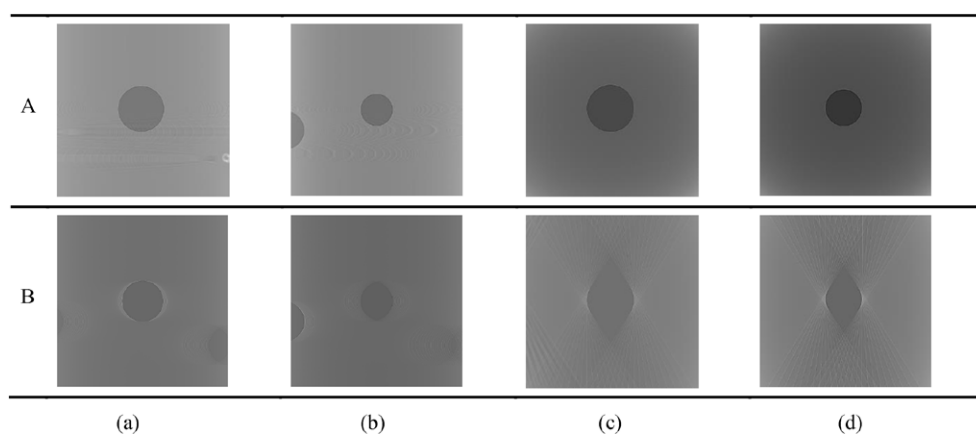
Figure 6. Comparison of ((a) and (b)) coronal and ((c) and (d)) axial reconstruction planes obtained from PhC projection images in (A) CT mode and (B) tomosynthesis mode at different depths in the reconstructed sphere: (a) and (c)—reconstructed slices corresponding to the central plane of the spherical object, (b) and (d) reconstructed slices corresponding to planes 2 mm away from the central plane. Inherent tomosynthesis artifacts are seen in images in (B).

The two algorithms can be applied using the same set of images. Each of them provides a look at object slices in a different way: SAA better produces flat regions and immediately reveals different-material regions. Flat regions still differ in the FBP reconstructions but in terms of mean intensity and to detect that difference, additional low-pass filtering would be required. FBP strongly enhances any edges (their magnitude is several orders stronger, see figures 5(a)–(d)) and can be used to detect the borders between the different materials and this is especially useful for the detection of very small objects (for example microcalcifications). Therefore, the authors consider the two algorithms as complementary, providing two different views without using additional radiation. Due to the limited scanning arc in tomosynthesis, volumetric reconstructions suffer worse resolution in a direction perpendicular to the coronary planes (planes that are parallel to the detector) (Sechopoulos 2013). The content presented on a coronary reconstruction image corresponds to a slice thicker than the pixels' width and height in the image and the thickness depends on the arc length. This is well seen in the axial reconstruction in figure 4 (the coronary planes are parallel to the image lines and perpendicular to the image plane). Only the central reconstructed plane (the one that passes through its center) reveals the sphere as a circular object in the tomosynthesis images. This is illustrated in figures 5(c) and (d), where one can observe the ovoid shape of the reconstructed sphere in a plane that is 2 mm away from the central plane for the case of the sphere in the middle of phantom 2. This is a known artifact for tomosynthesis using a circular scanning trajectory (Sarkar *et al* 2009) and it appears for PhC tomosynthesis imaging, as well.

Nevertheless, to additionally confirm that, the authors simulated the experimental PhC imaging setup and using a computer model of the paraffin phantom (figure 1, first row, second image), created PhC projection images and performed a series of CT and tomosynthesis reconstructions, following the methods adopted in a previous work (Bliznakova *et al* 2015). Coronal and axial reconstructions (by using FBP) are presented in figure 6.

The circular shape of the sphere cross-section is preserved in all reconstructed slices. The tomosynthesis images show the expected known artifacts.
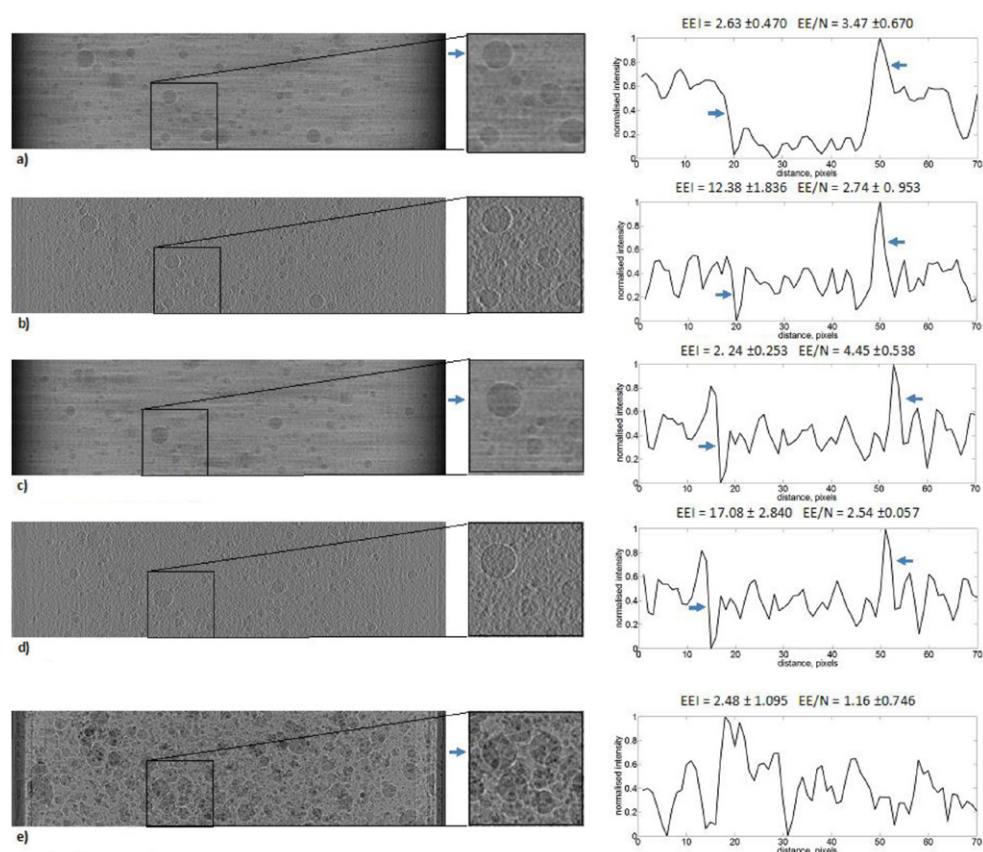
Figure 7. Comparison of PhC reconstructed tomosynthesis and planar images of the epoxy phantom (phantom 3) containing air sacs: selected tomosynthesis planes reconstructed with SAA ((a) and (c)) and FBP ((b) and (d)), respectively; (e) projection image corresponding to 0° (front view). The plotted profiles are taken horizontally across the largest spherical object in the ROI (short arrows are shown).

3.2. PhC tomosynthesis with phantoms composed of inhomogeneous background

3.2.1. Epoxy phantom (phantom 3). Figure 7 compares tomosynthesis slices reconstructed with SAA (figures 7(a) and (c)) and FBP (figures 7(b) and (d)), while figure 7(e) shows the image corresponding to the projection at 0° obtained in a PhC mode. On the same graph, plots of profiles taken horizontally across the ROIs (short arrows are shown) are presented.

The edge enhancement effect observed in the projection image of this inhomogeneous phantom is well preserved in all tomosynthesis images. The superposition of internal details (air sacs) produces a texture background well visible in the projection view; on the other hand, the reconstructed slices demonstrate partial removal of this complex background, showing fairly improved visibility for the details located in the corresponding plane, and well defined object dimensions and location. This visual result is well supported by the quantitative evaluation of the images. The calculated EEI is much higher for the slices reconstructed by FBP, as in the evaluated cases of phantom 1 and phantom 2, which are characterized by homogeneous backgrounds.

This experimental test showed the potential of PhC tomosynthesis for successfully resolving the complexity of a highly structured background in the x-ray imaging of thick and inhomogeneous phantoms, at least in cases with high-contrast details.
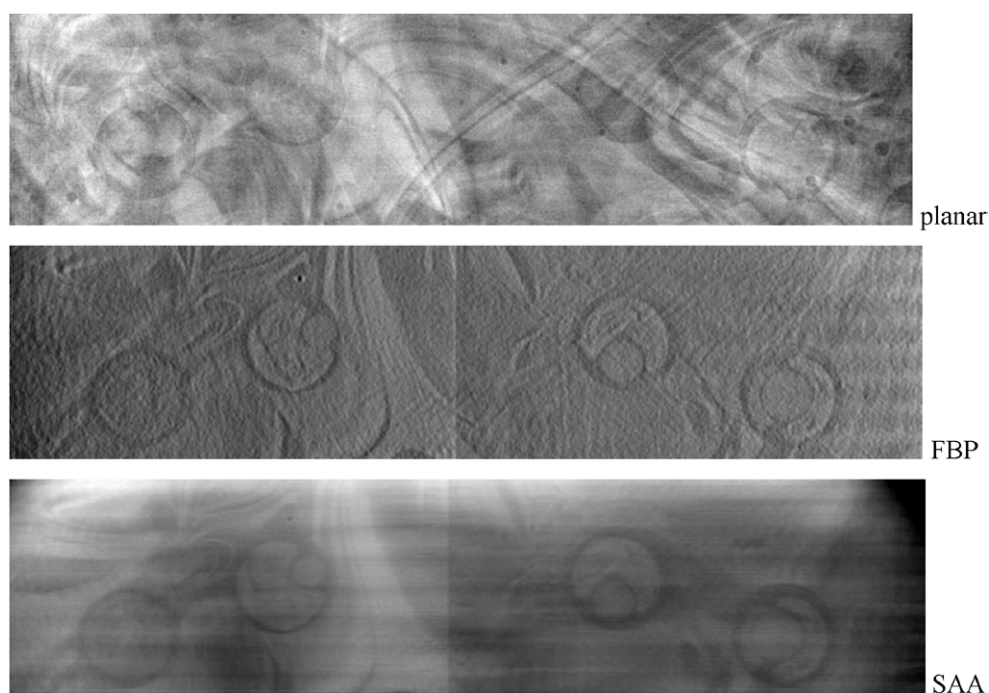
Figure 8. Comparison of ROI1, containing low-contrast details with size of 2.3 mm, 3.1 mm, 3.9 mm and 4.7 mm (from left to right), selected from the PhC planar image, and FBP and SAA reconstructed tomosynthesis images of the BR3D phantom (phantom 4).

3.2.2. Phantom 4. The results for phantom 4 are presented in figures 8–11. These figures show the reconstructed features in four selected ROIs contained in the BR3D commercial phantom: masses—ROI1 (figure 8), fibers—ROI2 and ROI3 (figures 9 and 10) and groups of micro-calcifications—ROI4 (figure 11), for the PhC planar image and reconstructed FBP and SAA tomosynthesis images. The projection and reconstruction images appear to mirror each other compared to the annotation of the ROIs in figure 1. As in the case of phantom 3, which is characterized by an inhomogeneous background, the simulated anatomical background, strongly present in the planar images (the top images in figures 8–11), is removed in the tomosynthesis images (second and third images in figures 8–11), thus leading to improved microcalcification and improved low-contrast visibility as well as the edge sharpness of these features.

A detailed comparison between the four ROIs taken from the planar and tomosynthesis images, shown in figures 8–11, reveals that most detail features are visible only in the tomosynthesis images (e.g. the groups of microcalcifications, the nylon fibers and the masses). For instance, in ROI4 from the planar image (figure 11), only microcalcifications with a grain size of 0.400 mm may be seen; similarly, in the images reconstructed with SAA this group of microcalcifications is also observed. By contrast, in the FBP reconstructed images, microcalcifications with sizes between 0.196 mm and 0.400 mm are well visualized. For these details, the contrast-to-noise ratio (CNR) and contrast were calculated and compared in table 2.

The CNR is higher for microcalcifications reconstructed with FBP, and their contrast is much improved. This is explained by the high-frequency nature of the filter used to pre-process the projection images in the FBP, which gives rise to the high-frequency content amplification. Similar results are reported from the task-based evaluation for the microcalcifications,

Figure 9. Comparison of ROI2, containing nylon fibers with diameters 0.12 mm, 0.28 mm and 0.41 mm (from left to right), selected from the PhC planar image, and FBP and SAA reconstructed tomosynthesis images of the BR3D phantom (phantom 4).
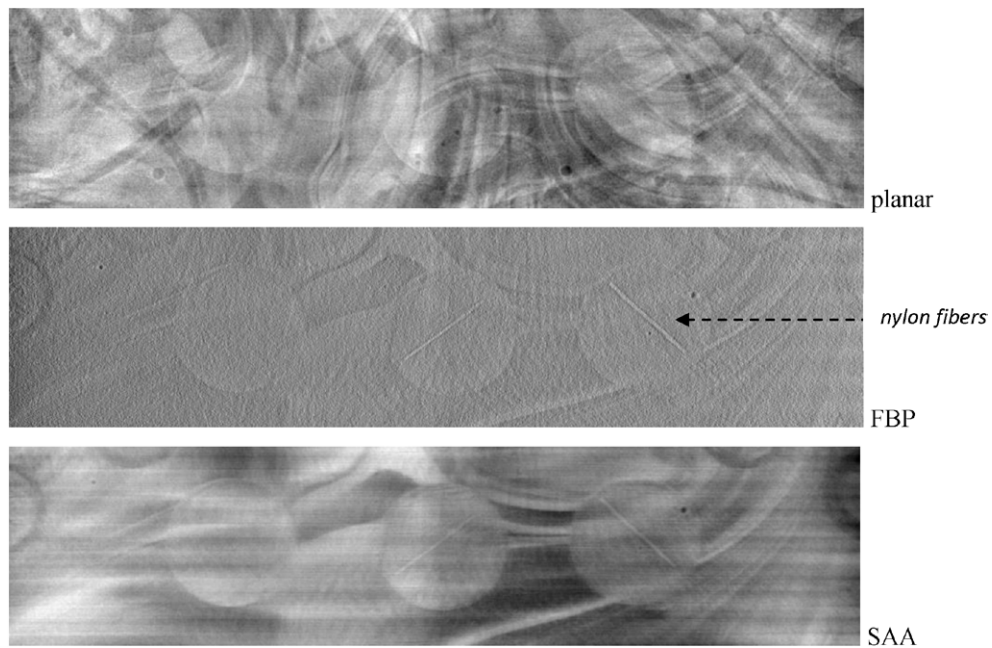

Figure 10. Comparison of ROI3, containing nylon fibers with diameters 0.15 mm, 0.23 mm, 0.38 mm and 0.60 mm (from left to right), selected from the PhC planar image, and FBP and SAA reconstructed tomosynthesis images of the BR3D phantom (phantom 4).
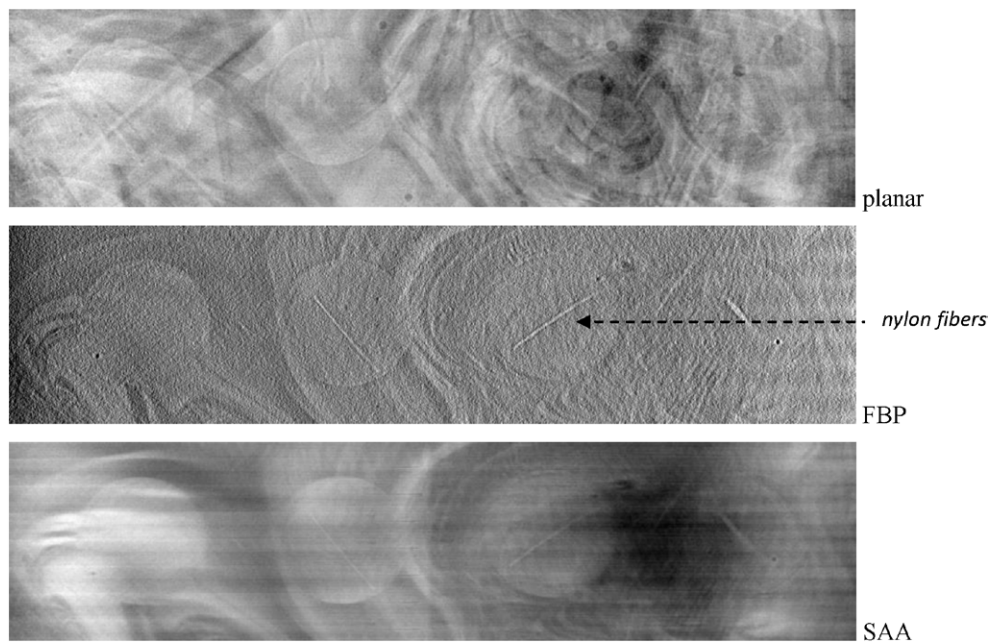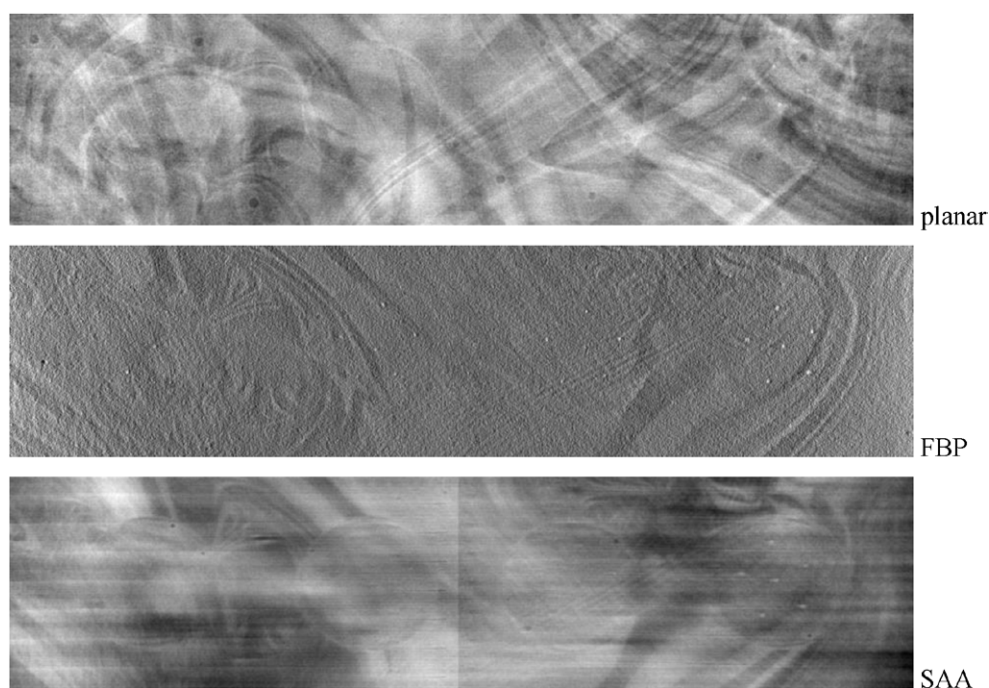
Figure 11. Comparison of ROI4, containing groups of microcalcifications of different sizes, selected from the PhC planar image, and FBP and SAA reconstructed tomosynthesis images of the BR3D phantom (phantom 4).

Table 2. Detail contrast and contrast-to-noise ratio for the four groups of microcalcifications, calculated on planar and reconstructed images.

Modality	Parameter	Microcalcification size			
		0.400 mm	0.290 mm	0.230 mm	0.196 mm
Planar	CNR	2.76 ± 0.682	[a]	[a]	[a]
	$C, \%$	42.25 ± 10.443	[a]	[a]	[a]
SAA	CNR	4.45 ± 1.227	[a]	[a]	[a]
	$C, \%$	1.02 ± 0.282	[a]	[a]	[a]
FBP	CNR	5.05 ± 0.666	5.02 ± 1.07	4.85 ± 0.503	2.97 ± 0.408
	$C, \%$	98.38 ± 12.978	93.87 ± 19.993	83.78 ± 8.690	58.44 ± 8.041

[a] Not measured since microcalcifications were not visible.

summarized in table 3. Microcalcifications with size of 0.196 mm may be clearly seen on the FBP images, while this is not the case for the planar and SAA images.

Similar results were observed for the nylon fibers present in ROI2 and ROI3 (figures 9 and 10). From the nylon fibers, which had a length of 10 mm, the fibers with diameters in the range between 0.6 mm and 0.23 mm (ROI3) as well as between 0.28 mm and 0.41 mm (ROI2) were slightly visible on the projection images. In contrast, these fibers were well defined in both the SAA and FBP reconstructed images. These fibers were not visible on the projection image mainly due to the inhomogeneous background containing tissue simulating materials with properties close to the absorption properties of real breast tissue. Line

Table 3. Results from the task-based evaluation applied for ROI4 (groups of microcalcifications). The number of microcalcifications seen per group is given in brackets.

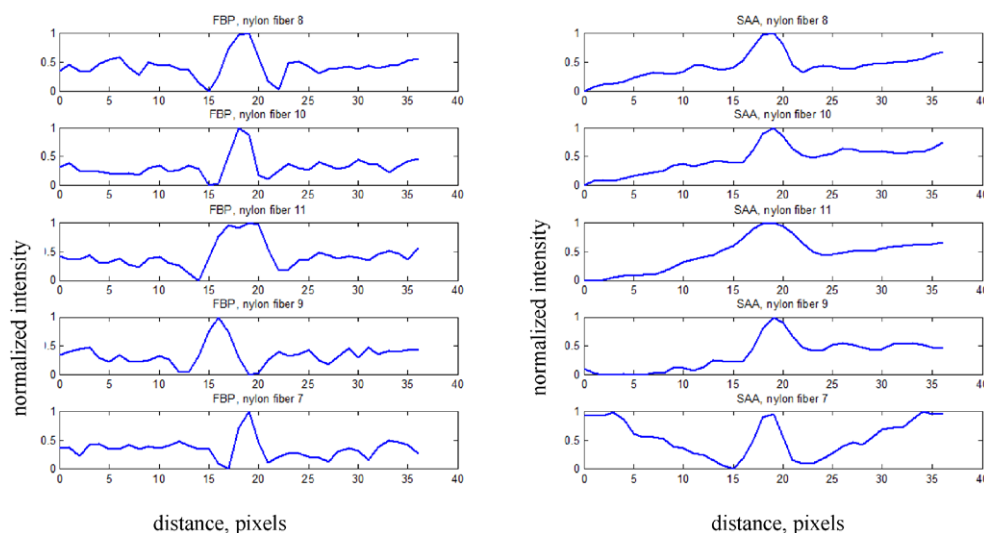| Modality	Observer	Group 1 0.196 mm	Group 2 0.230 mm	Group 3 0.290 mm	Group 4 0.400 mm	Ranking of the modality
Planar	1	1(0)	1(0)	1(0)	3(3)	3
	2	1(0)	1(0)	2(1)	3(6)	3
	3	2(1)	1(0)	3(4)	4(3)	3
FBP	1	2(2)	3(5)	4(6)	5(6)	1
	2	3(5)	4(6)	5(6)	5(6)	1
	3	3(6)	4(6)	5(6)	5(6)	1
SAA	1	1(0)	2(1)	2(1)	2(5)	2
	2	1(0)	1(1)	1(3)	5(6)	2
	3	1(0)	2(1)	2(3)	4(6)	2

Figure 12. Comparison of nylon fibers with the following diameters: fiber 7—0.6 mm, fiber 8—0.41 mm, fiber 9—0.38 mm, fiber 10—0.28 mm, fiber 11—0.23 mm. ROI4 selected from the PhC planar image, and the FBP and the SAA reconstructed PhC tomosynthesis images of the BR3D phantom (phantom 4).

profiles were taken across these fibers and compared in figure 12. The comparison of the line profiles shows sharper edges of the nylon fibers reconstructed with FBP in comparison with those reconstructed with SAA. This observation supports well the improved nylon fiber appearance in FBP images compared to that in SAA images. The task-based evaluation, summarized in table 4, shows an advantage for the FBP images, followed by the SAA and the planar images. Nylon fibers were almost invisible on the planar images as the highest score in this case was 2, which corresponds to 'probably absent'. The observers noted that both the FBP and the SAA gave similar results; however, they preferred FBP due to the improved edge visibility.

Finally, masses are well visualized in both the SAA and FBP tomosynthesis compared to masses in the planar images. Indeed, masses in the planar image of ROI1 (figure 8) are not

Table 4. Results from the task-based evaluation applied for ROI2–3 (nylon fibers).

Modality	Observer	Fibers 0.18 mm	Fibers 0.28 mm	Fibers 0.41 mm	Fibers 0.15 mm	Fibers 0.23 mm	Fibers 0.38 mm	Fibers 0.60 mm	Ranking of modality
Planar	1	1	1	1	1	2	1	1	3
	2	1	1	4	1	4	1	1	3
	3	1	1	2	1	2	2	2	3
FBP	1	1	5	5	1	5	5	3	1
	2	1	5	5	1	5	5	4	1
	3	2	5	5	3	3	5	5	1
SAA	1	1	3	4	1	3	4	3	2
	2	1	5	5	1	5	5	4	2
	3	1	5	5	1	5	5	5	2

Table 5. Detail contrast and contrast-to-noise ratio for the four spheroidal masses, calculated on reconstructed images.

Modality	Parameter	Spheroidal mass size			
		2.3 mm	3.1 mm	3.9 mm	4.7 mm
SAA	CNR	1.60	16.92	0.76	1.21
	$C, \%$	1.59	1.27	0.07	1.34
FBP	CNR	[a]	0.44	0.26	0.28
	$C, \%$	[a]	49.39	58.56	40.92

[a] Not measured since masses were not visible.
Note: Masses on planar images were not visible.

Table 6. Results from the task-based evaluation applied for ROI1 (masses).

Modality	Observer	Mass 2.3 mm	Mass 3.1 mm	Mass 3.9 mm	Mass 4.3 mm	Ranking of modality
Planar	1	1	1	1	1	3
	2	1	1	1	3	3
	3	1	1	1	1	3
FBP	1	1	5	5	5	2
	2	1	5	5	5	2
	3	1	5	5	4	2
SAA	1	1	5	5	5	1
	2	3	5	5	5	1
	3	1	5	5	4	1

visible at all. These are hemispherical masses with diameter between 2.3 mm and 4.7 mm. Quantitatively, their CNR and contrast were evaluated and listed in table 5.

As expected, masses reconstructed with SAA have higher CNRs than those with FBP. This has already been demonstrated in a previous study at a synchrotron facility (Bliznakova *et al* 2010). The random and structured noise in the images is related to the high-frequency components in the spectra of the images. SAA acts as a low-pass filter for out-of-plane content, while the FBP excludes that content and this results in a lower CNR compared to SAA. The results from the quantitative assessment are well supported by the results of the task-based

evaluation, summarized in table 6. The observers ranked the planar images on third place, while they evaluated SAA to be better at reconstructing masses than FBP. In addition, they all agreed that low-contrast features were absent or probably absent on the planar images.

Overall, low-contrast large-area details, such as masses, are well reconstructed with SAA compared to FBP. The anatomical structured noise is fairly reduced and the masses are well visualized, despite the blurring effects present on the image. In the case of FBP, in-plane and out-of-plane low-frequency content is suppressed. This combined with the high-frequency noise in the reconstructed images leads to lower CNR values for the masses reconstructed by FBP in comparison to those reconstructed by SAA. Therefore, FBP combined with the Ram–Lak filter is a suitable algorithm for reconstructions of high-contrast features like micro-calcifications. In this case, the high-frequency content is amplified and at the same time the heterogeneous background is well suppressed, which results in higher CNR values for micro-calcifications compared to those reconstructed with SAA.

Similar to x-ray projection mammography, PhC projection imaging lacks depth-of-focus information. When imaging thick, complex specimens (as in the case of phantom 3) or entire breast phantoms (as in the case of phantom 4), the superposition of various features present in the sample complicates the image interpretation task. The use of 3D techniques, like digital tomosynthesis, overcomes at least in part these limitations. The current study showed the ability to improve the detection task: to precisely characterize the location and dimensions of objects within the phantom, as well as to preserve the edge enhancement that is observed in planar PhC projection images. The images shown were obtained with an in-line PhC setup. The in-line method is the simplest and most adopted technique for PhC imaging, since it does not require the use, in the imaging setup, of any optics or grating elements between the sample and the detector, in order to perform wave splitting or any kind of image reconstruction.

The transfer of this imaging modality for breast imaging with monochromatic radiation to the clinical environment is being pioneered at the Elettra synchrotron facility (Trieste, Italy) (Arfelli *et al* 2000), with demonstration of higher contrast in PhC images than in absorption images with a synchrotron in the energy range of 15 keV and 25 keV, for breast tissue specimens. Preliminary results with patients examined on both synchrotron and conventional mammography units indicated that from the diagnostic point of view, PhC synchrotron images are never inferior to those from conventional units (Castelli *et al* 2007, 2011, Dreossi *et al* 2007, 2008). Recently at this infrastructure, detail quantitative evaluation and optimization of PhC CT have been accomplished with respect to the detection of small tumors in breast tissue (Gureyev *et al* 2014). In this framework, on the basis of the findings of this work, synchrotron DBT has potential for further improving the diagnostic task of lesion detection.

The experimental study was carried out at ID17 at the ESRF, a beamline which has at its disposal a suitable large-area detector. The closest possible distance between the detector and the object in PhC mode was approximately 6 m. Nowadays, this study could be successfully completed at the SYRMEP beamline at Elettra, for example at a distance of 166 cm (the longest available distance) and with a large-area detector. Recently, PhC CT was successfully applied at this beamline (Gureyev *et al* 2014). The authors evaluated both propagation-based and analyzer-based PhC imaging combined with CT for two plastic phantoms and four excised breast samples. Appropriate conditions for realization of this technique may include the medical beamline of the Australian Synchrotron, which has a large-area detector and distant object-detector that could be adjusted up to 5 m (Nesterets *et al* 2015).

In the present study, images were reconstructed by backprojection algorithms, which were already implemented in the reconstruction platform. However, these algorithms are characterized by some imperfections like streaking artifacts, shadowing around dense reconstructed objects and other noise-like textures. These artifacts may obscure some of the fine anatomical

details of the image. Over the last five years, much effort has been made at developing and modifying existing iterative reconstruction techniques applied to PhC images. Among these algorithms are the statistical iterative algorithm (Fahimian *et al* 2010, Hahn *et al* 2015), an iterative algorithm based on the Fourier transform (Cong *et al* 2012), the algebraic reconstruction method (Fu *et al* 2015), and an iterative algorithm based on the penalized maximum likelihood reconstruction algorithm (Brendel *et al* 2016). In all cases, image quality is significantly improved in comparison to the FBP method. Therefore, a continuation of this work will concern the realization of iterative algorithms and their use with the available image sets. It is also planned for these algorithms to be applied using projections obtained from in-house developed anthropomorphic breast phantoms (Bliznakova *et al* 2016) and breast tissue samples.

For the setup at beamline ID17 at the ESRF, the time for obtaining an image with a height of 6 mm and a width of 150 mm was 26 ms. For an image with a height of 18 cm, the needed time for exposure for 17 images in a tomosynthesis arc will be 13.26 s, which is almost double that for conventional breast tomosynthesis (Qian *et al* 2012). In these calculations, the time needed for platform movement in the z direction has not been taken into account. The needed time would depend on the used setup, and the detector size and properties and it is also subject to optimization, since the number of images may be decreased and the resolution of the detector could be lower than that used in the study.

4. Conclusions

The SAA and FBP algorithms were successfully tested for PhC tomosynthesis. This experimental phantom study showed that features were well differentiated and characterized on tomosynthesis images. In addition, their edges were still sharp, as in the planar case. It is important that PhC tomosynthesis was capable of preserving enhanced edges in the reconstructed images especially for thick and inhomogeneous phantoms. Edge visibility was much improved when using FBP, which resulted in a much better subjective (visual) determination of the contours of the details of interest. However, images reconstructed with SAA looked more similar to the classic tomographic images and provided a better perception for the reconstructed tissues. In this sense, the two reconstruction algorithms can be considered as complementary reconstruction techniques for evaluating more complex phantoms. From a clinical perspective, in-line PhC breast tomosynthesis might improve the task of detection of suspicious areas in mammography images by adding the edge enhancement effect (due to PhC) to reconstructed attenuation images. Further investigations will be devoted to the validation of the presented findings by imaging *ex vivo* breast samples and elaboration of the current SAA and FBP algorithms to improve reconstructions of objects from PhC images.

Acknowledgments

Conflict of interest statement

None declared.

References

Arfelli F *et al* 2000 Mammography with synchrotron radiation: phase-detection techniques *Radiology* **215** 286–93

Berger M J, Hubbell J H, Seltzer S M, Chang J, Coursey J S, Sukumar R, Zucker D S and Olsen K 2010 *XCOM: Photon Cross Section Database (Version 1.5)* (Gaithersburg, MD: National Institute of Standards and Technology) (Available: http://physics.nist.gov/xcom)

Bliznakova K, Kolitsi Z, Speller R D, Horrocks J A, Tromba G and Pallikarakis N 2010 Evaluation of digital breast tomosynthesis reconstruction algorithms using synchrotron radiation in standard geometry *Med. Phys.* **37** 1893–903

Bliznakova K, Mettivier G, Russo P and Buliev I 2016 Contrast detail phantoms for x-ray phase-contrast mammography and tomography *IWDM Malmo (18–22 June 2016)* (Switzerland: Springer)

Bliznakova K, Russo P, Mettivier G, Requardt H, Popov P, Bravin A and Buliev A 2015 A software platform for phase contrast x-ray breast imaging research *Comput. Biol. Med.* **61** 62–74

Bravin A, Mocella V, Coan P, Astolfo A and Ferrero C 2007 A numerical wave-optical approach for the simulation of analyzer-based x-ray imaging *Opt. Express* **15** 5641–8

Brendel B, von Teuffenbach M, Noel P B, Pfeiffer F and Koehler T 2016 Penalized maximum likelihood reconstruction for x-ray differential phase-contrast tomography *Med. Phys.* **43** 188–94

Castelli E *et al* 2007 Clinical mammography at the SYRMEP beam line *Nucl. Instrum. Methods* A **572** 237–40

Castelli E *et al* 2011 Mammography with synchrotron radiation: first clinical experience with phase-detection technique *Radiology* **259** 684–94

Cong W X, Momose A and Wang G 2012 Fourier transform-based iterative method for differential phase-contrast computed tomography *Opt. Lett.* **37** 1784–6

Donnelly E F, Lewis K G, Wolske K M, Pickens D R and Price R R 2006 Characterization of the phase-contrast radiography edge-enhancement effect in a cabinet x-ray system *Phys. Med. Biol.* **51** 21–30

Dreossi D *et al* 2007 Clinical mammography at the SYRMEP beam line: toward the digital detection system *Nucl. Instrum. Methods* A **576** 160–3

Dreossi D *et al* 2008 The mammography project at the SYRMEP beamline *Eur. J. Radiol.* **68** S58–62

Durand M A, Haas B M, Yao X, Geisel J L, Raghu M, Hooley R J, Horvath L J and Philpotts L E 2015 Early clinical experience with digital breast tomosynthesis for screening mammography *Radiology* **274** 85–92

Fahimian B P, Mao Y, Cloetens P and Miao J W 2010 Low-dose x-ray phase-contrast and absorption CT using equally sloped tomography *Phys. Med. Biol.* **55** 5383–400

Friedewald S M, Rafferty E A and Conant E F 2014 Breast cancer screening with tomosynthesis and digital mammography-reply *J. Am. Med. Assoc.* **312** 1695–6

Fu J, Hu X H, Velroyen A, Bech M, Jiang M and Pfeiffer F 2015 3D algebraic iterative reconstruction for cone-beam x-ray differential phase-contrast computed tomography *PLoS One* **10** e0117502

Guan H, Xu Q, Garson A and Anastasio M A 2014a *Medical Imaging 2014: Physics of Medical Imaging* vol 9033 (San Diego, CA: SPIE)

Guan H F, Xu Q F, Garson A and Anastasio M A 2014b Depth resolution properties of in-line x-ray phase-contrast tomosynthesis *Medical Imaging 2014: Physics of Medical Imaging* **9033** 90330H

Gureyev T E *et al* 2014 Investigation of the imaging quality of synchrotron-based phase-contrast mammographic tomography *J. Phys. D: Appl. Phys.* **47** 365401

Hahn D, Thibault P, Fehringer A, Bech M, Koehler T, Pfeiffer F and Noel P B 2015 Statistical iterative reconstruction algorithm for x-ray phase-contrast CT *Sci. Rep.* **5** 10452

Hammonds J C, Price R R, Donnelly E F and Pickens D R 2011 Phase-contrast digital tomosynthesis *Med. Phys.* **38** 2353–8

Ikeya A, Teramoto A, Noguchi K and Fujita H 2013 *Medical Imaging 2013: Physics of Medical Imaging (Lake Buena Vista, FL)* vol 8668

Kamarianakis Z, Buliev I and Pallikarakis N 2013 A C++ platform for image reconstruction in x-ray imaging *5th Panhellenic Conf. on Biomedical Technologies, ELEVIT (Athens, Greece)*

Kamarianakis Z, Buliev I and Pallikarakis N 2014 A platform for image reconstruction in x-ray imaging: medical applications using CBCT and DTS algorithms *CSJM* **22** 236–52

Kolitsi Z, Panayiotakis G, Anastassopoulos V, Scodras A and Pallikarakis N 1992 A multiple projection method for digital tomosynthesis *Med. Phys.* **19** 1045–50

Kopans D B 2014 Digital breast tomosynthesis from concept to clinical care *Am. J. Roentgenology* **202** 299–308

Li K, Ge Y, Garrett J, Bevins N, Zambelli J and Chen G H 2014 Grating-based phase contrast tomosynthesis imaging: proof-of-concept experimental studies *Med. Phys.* **41** 011903

Nesterets Y I *et al* 2015 A feasibility study of x-ray phase-contrast mammographic tomography at the imaging and medical beamline of the Australian synchrotron *J. Synchrotron Radiat.* **22** 1509–23

Qian X *et al* 2012 High resolution stationary digital breast tomosynthesis using distributed carbon nanotube x-ray source array *Med. Phys.* **39** 2090–9

Sarkar V, Shi C, Rassiah-Szegedi P, Diaz A, Eng T and Papanikolaou N 2009 The effect of a limited number of projections and reconstruction algorithms on the image quality of megavoltage digital tomosynthesis *J. Appl. Clin. Med. Phys.* **10** 2970

Sarno A, Mettivier G and Russo P 2015 Dedicated breast computed tomography: basic aspects *Med. Phys.* **42** 2786–804

Schleede S *et al* 2014 X-ray phase-contrast tomosynthesis for improved breast tissue discrimination *Eur. J. Radiol.* **83** 531–6

Sechopoulos I 2013 A review of breast tomosynthesis. Part I. The image acquisition process *Med. Phys.* **40** 014301

Szafraniec M B, Millard T P, Ignatyev K, Speller R D and Olivo A 2014 Proof-of-concept demonstration of edge-illumination x-ray phase contrast imaging combined with tomosynthesis *Phys. Med. Biol.* **59** N1–10